Better understanding of solar water evaporation systems using a biosourced foam and its modelling

R Fillet, Vincent Nicolas, A Celzard, Vanessa Fierro

BETTER UNDERSTANDING OF SOLAR WATER EVAPORATION SYSTEMS USING A BIOSOURCED FOAM AND ITS MODELLING

R. Fillet, V. Nicolas*, A. Celzard, V. Fierro*

Université de Lorraine, CNRS, IJL, F-88000 Epinal, France

*Corresponding Author: vincent.nicolas@univ-lorraine.fr

*Corresponding Author: vanessa.fierro@univ-lorraine.fr

ABSTRACT

A two-dimensional axisymmetric finite element model of a solar evaporator based on a tannin foam has been developed using COMSOL Multiphysics. This model includes a set of boundary conditions and mass transfer within the porous structure. Experiments were conducted to validate the model as the parameters changed over time. Using the model, the effects of light absorption at the surface, water diffusion inside the material, and the thickness of the material and the insulating wall were investigated. We showed that a 38% decrease in evaporation rate was observed when water diffusion does not allow sufficient transport of water to the surface. In addition, an increase in light absorption from 0.8 to 0.9 increases the evaporation performance by 12% and insulation of the exterior does not yield significant changes. A final section of the article focuses on the temporal evolution of water evaporation in several locations around the world. We concluded that hot and dry climates have the highest evaporation potential. Among the cities studied, the highest theoretical evaporation for this biosourced foam was predicted for Dubai, 5342 $kg.m^{-2}$, followed by Cairo, 4723 $kg.m^{-2}$.

Keywords: Simulation; Biosourced material; Solar energy; Solar evaporation; Porous media; Heat and mass transfers

42

Nomenclature

a	[-]	Water activity
c_p	[J K^{-1} kg^{-1}]	Heat capacity
D	[m^2 s^{-1}]	Coefficient of diffusion of water inside the material
E	[-]	Emissivity of the material and of the side of the beaker
h_c	[W m^{-2} K^{-1}]	Heat transfer coefficients
h_v	[kJ.kg^{-1}]	Enthalpy of vaporisation
H_R	[-]	Relative humidity
k	[m.s^{-1}]	Convective mass exchange coefficient
M	[kg mol^{-1}]	Molar mass of water
P	[Pa]	Pressure
$P_{s,0}$	[W.m^{-2}]	Average solar illumination
R	[J mol^{-1} K^{-1}]	Universal gas constant
T	[K]	Temperature
T_{ref}	[K]	Reference temperature

Special characters

ε	[-]	Volume fraction
λ	[W m^{-1} K^{-1}]	Thermal conductivity
φ	[-]	Porosity
ρ	[kg m^{-3}]	Density
η	[-]	Efficiency
σ	[W m^{-2} K^{-4}]	Stefan-Boltzmann constant
τ_o	[-]	Tortuosity

Subscripts

a	Ambient
b	Bottom
i	Component i
m	Material
s	Side
sat	Saturation
v	Vaporisation
w	Water
0	Reference

43

44

45

1 INTRODUCTION

Due to global warming, increasing world population and river pollution, drinking water resources will become scarcer in the coming years. By 2050, 3.9 billion people, or more than 40% of the world's population, will be living in watersheds under severe water stress [1]. To solve this problem, in addition to reducing consumption, several complementary approaches could be developed, including storage and/or recovery and treatment of water unsuitable for consumption.

One of the water purification strategies is direct evaporation by a passive evaporation system, using solar energy to recover salty and/or polluted water. Indeed, some materials called photothermal, once placed on the surface of water, have the ability to absorb solar energy and accelerate its evaporation, thus transforming between 80 % and 90 % of the solar energy received into water vapour [2]. Water evaporation systems improve evaporation compared to a system without materials and therefore have attracted much attention and a wide variety of materials have been developed [3].

Heat transfer is the driving force of the evaporation phenomenon and its study is the key to optimize performance of the evaporation process [4–6]. A water evaporation system consists of a material that has high absorption of light radiation to allow maximum utilisation of the incoming energy. In the literature, three configurations have been proposed. The first configuration consists of an absorbing material placed at the bottom of the water [7,8]. In the second configuration, the material is dispersed in the water as a powder, giving a black tint to the bulk water [2,9]. In the last and most efficient configuration, the material is placed on top of the bulk water. In this case, after absorption of sunlight, the heat must remain at the top of the material, where evaporation occurs, to increase the surface temperature and thus the vapour pressure. To keep the heat at the evaporative surface, thermal insulation is placed between the bulk water and the evaporative material [10]. In this case,

thin materials such as cotton or other water transport media can be used to transfer the bulk water to the evaporation interface [11]. Therefore, the thin material is placed on an insulating layer to allow it to float and increase the evaporation rate [12,13]. Alternatively, some materials such as wood show good insulating and water transport properties, and they can be placed in direct contact with bulk water. By using India ink to enhance the sunlight absorption of basswood, a production of 1.6 $kg.m^{-2}.h^{-1}$ under 1 sun illumination was achieved [14]. Another example achieved 1.5 $kg.m^{-2}.h^{-1}$ under 1 sun illumination with a flame-treated coconut [15]. 3D structures have also been used to increase the exchange area with reported values higher than 10 $kg.m^{-2}.h^{-1}$ [16,17]. Although numerical simulations have been implemented for solar evaporation systems [18–20], they have been limited to verifying certain aspects of their design, such as temperature distribution, airflow velocity, water diffusion or geometry.

Most of the studies reported in the open literature focus on the development of materials from a chemical or structural point of view without addressing the impact of material properties on the overall performance. In order to understand the phenomena undergone and to optimise these systems, a two-dimensional axisymmetric model of a tannin-based foam solar evaporator was developed in a previous study [21], including a set of boundary conditions and water transport in the porous medium. The latter study helped to validate the previously recommended conditions for measuring evaporation performance [22], namely an air temperature of about 25 °C and a relative humidity of less than 60 %.

The present study utilises the previously used tannin foam with an optimised configuration. In our previous study [21], the foam was placed directly on top of liquid water, whereas here the foam is placed on top of an insulator to limit the downward heat loss and increase the surface temperature of the foam. The previous model has been modified accordingly and is used to study specific material properties, such as sunlight absorption, water transport and thickness of the porous

93 structure and the insulating wall. In a first step, the validation of the model against the experimental
94 data is performed with a cyclic evolution of lighting conditions to simulate the day and night phases
95 and, in a second step, a parametric study is performed on the material properties and the geometry
96 of the system. Finally, a temporal study of evaporation during a summer day for the city of Paris is
97 performed. This is followed by the determination of water evaporation over a full year and the
98 study of the impact of latitude, temperature and relative humidity for several cities around the world
99 using our tannin-derived foam.
100

101 # 2 MATERIALS AND METHODS

102 ## 2.1 EVAPORATION MATERIAL

103 The tannin used to produce the foam was extracted from the bark of the mimosa tree (*Acacia*
104 *Mearnsii)* using an industrial process, and the synthesis of the foam from this tannin is described
105 elsewhere [23,24]. The foam was then cut to the appropriate size (58 mm diameter and 2 mm thick)
106 and can be seen in **Figure 1**.
107

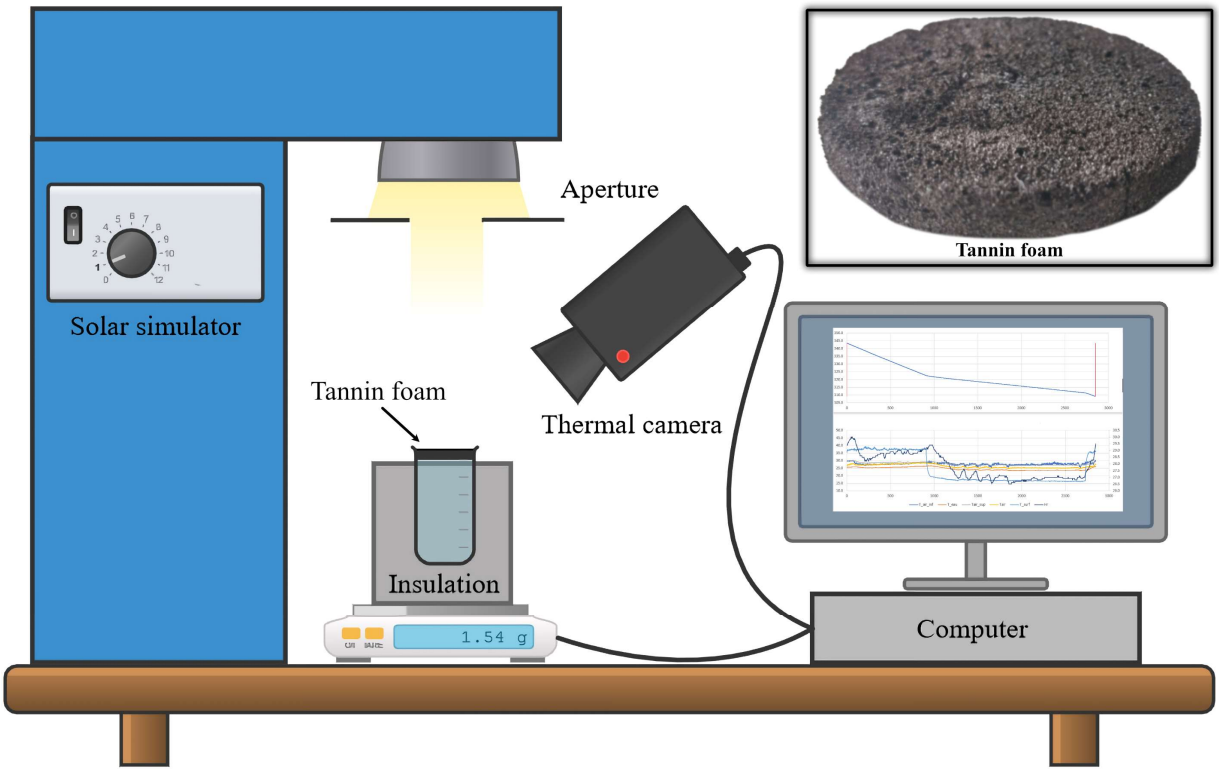

Figure 1. Experimental setup with a photo of the tannin foam in the upper right frame.

2.2 EXPERIMENTAL PROTOCOL AND MEASUREMENT METHODS

The experiments were conducted using a solar light simulator (SOLAR LIGHT LS-1000) to illuminate a beaker (60 mm diameter) filled with distilled water: see **Figure 1**. The tannin foam was on a cotton layer wrapped around a polystyrene foam for insulation between the evaporation and water surfaces. The system was placed on a Sartorius ENTRIS balance accurate to the milligram to monitor the overall mass of the system and thus the evaporation rate. In addition, a thermal camera (OPTRIS PI) pointing to the top of the beaker was used to measure the surface temperature. Ambient temperature and humidity conditions were also monitored during the experiment using a sensor placed in the room. The solar simulator was first calibrated to deliver

1000 W.m^{-2} of solar light and the beaker was wrapped with the insulation layer and filled with water and, the evaporation system was placed on its surface. It was then positioned on the balance to record the evolution of the water mass over two six-hour cycles (**Figure 2a**), during which the sunlight was switched on for the first three hours and off for the last three hours. The evolution of the mass over time was used to calculate the evaporation rate and to compare the experimental results to those predicted by the numerical model. The evolution of heat and mass could thus be followed with the variation of the solar concentration.

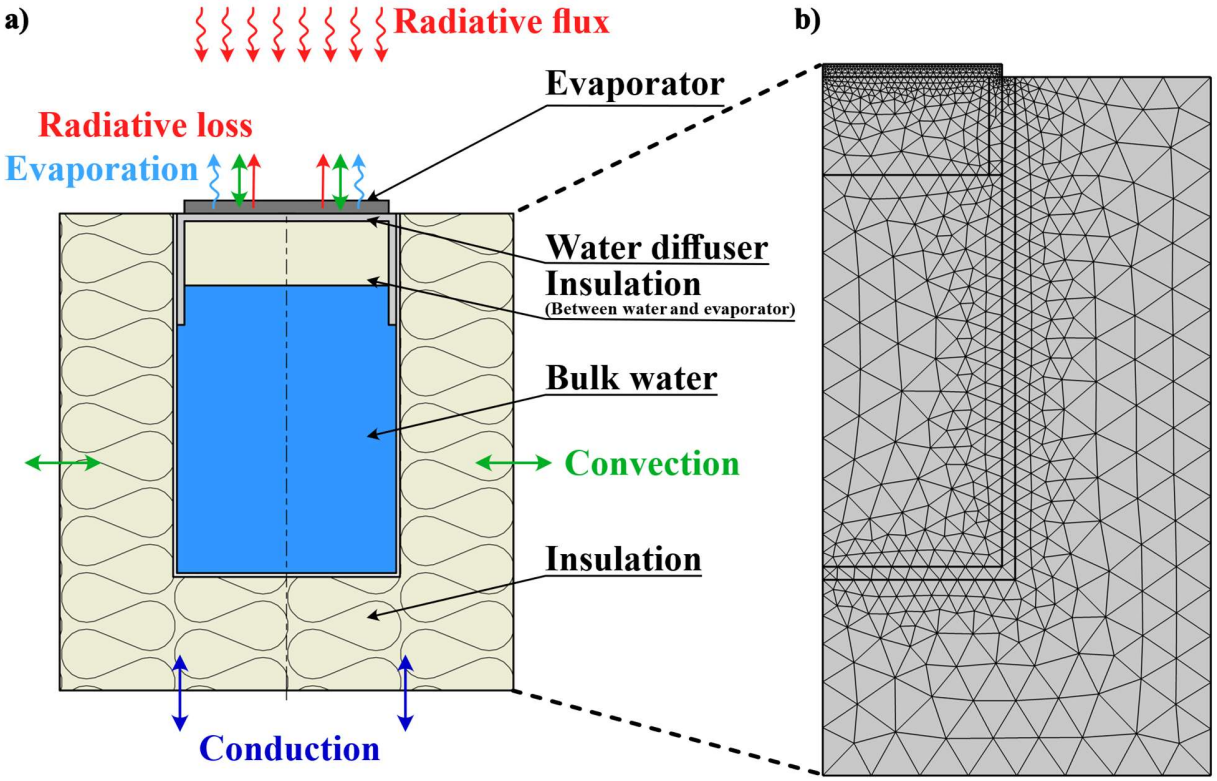

Figure 2. a) Types of heat exchange at the boundaries of the water evaporation system and b) mesh used for the numerical simulation.

The overall system efficiency was calculated using Eq.1.

$$\eta = \frac{\dot{m}[h_v + c_{p,v}(T - T_{ref})]}{P_s} \qquad \textbf{Eq. 1}$$

with h_v the vaporisation enthalpy (kJ.kg^{-1}), $c_{p,v}$ the thermal capacity of water vapour (J.kg^{-1}.K^{-1}), T_{ref} the reference temperature (273.15 K), P_s (W.m^{-2}) the sunlight power on earth per unit area and $\dot{m}$ (kg.m^{-2}.h^{-1}) the evaporation rate, calculated as follows :

$$\dot{m} = \frac{1}{S_i} \int_0^{S_e} F_m dS \qquad \textbf{Eq. 2}$$

with S_i (m^2) the projected area that is irradiated by sunlight, S_e (m^2) the evaporation surface and F_m the boundary mass flux calculated later in Eq.10.

In the literature, a typical result is an evaporation rate coupled with an efficiency, for a given solar energy concentration. Theoretically, an efficiency of 100 %, knowing that the enthalpy of evaporation of water is 2450 kJ.kg^{-1} (at standard temperature and pressure), gives an evaporation rate $\dot{m}$ of 1.47 kg.m^{-2}.h^{-1} for a received solar energy of 1 sun. This represents the theoretical evaporation limit for these conditions, if the material were perfect. It should be noted, however, that this does not take into account the thermal exchanges with the exterior.

2.3 PHYSICAL AND NUMERICAL MODEL

COMSOL 6.0 was used to build a 2D axisymmetric model of the system. Rectangles were used to model the bulk material and water (red and blue in **Figure 2**, respectively). Heat transfers occur in the overall geometry while mass transfers occur only in evaporative material. Boundary conditions at the surface include solar illumination, air convection and water evaporation. Air convection occurs at the sides and conduction occurs at the bottom. All input parameters used for the system simulation are gathered in **Table 1.**

2.3.1 General equations for the evaporative material

The mass transfer was described by the diffusion of water into the material. A transient equation was used to allow the material to dry out and thus reduce surface evaporation when it is no longer saturated. This equation was obtained by maintaining liquid water inside the material (Eq. 3).

$$\boldsymbol{\rho_w \frac{\partial \varepsilon_l}{\partial t} + \vec{\nabla}.\left(\overrightarrow{\dot{m}_w} + \overrightarrow{\dot{m}_v}\right) = -\frac{\partial(\varepsilon_g \rho_v)}{\partial t}} \quad \textbf{Eq. 3}$$

where ε_l is the liquid volume fraction, ε_g is the gas fraction, ρ_w is the density of liquid water (kg.m^{-3}), ρ_v is the density of vapour (kg.m^{-3}) and $\dot{m}_w$ and $\dot{m}_v$ are the mass fluxes of water and vapour (kg.m^{-2}.s^{-1}), such as :

$$\boldsymbol{\overrightarrow{\dot{m}_w} = -\rho_w D_w \vec{\nabla} \varepsilon_l} \quad \textbf{Eq. 4}$$

$$\boldsymbol{\overrightarrow{\dot{m}_v} = -\rho_g \frac{D_v \varepsilon_g}{\tau_o \varphi} \vec{\nabla} \frac{\rho_v}{\rho_g}} \quad \textbf{Eq. 5}$$

where ρ_g is the density of gas defined as a mixing of dry air and vapour at atmospheric pressure (kg.m^{-3}), D_w (m².s^{-1}) is the diffusion coefficient of water in the material, D_v (m².s^{-1}) is the diffusion coefficient of vapour in the air, φ (dimensionless) is the porosity of the material and τ_o (dimensionless) the tortuosity of the material.

The heat and mass transfer that occurs during the evaporation process was simulated using two state variables, the temperature, *T,* and the volume fraction of liquid in the pores, ε_l, with the energy and mass conservation equations (Eq. 3 and Eq. 6, respectively). The energy associated with mass transfer was assumed to be negligible due to the very slow kinetics of this phenomenon.

$$\boldsymbol{\rho_m c_{p,m} \frac{\partial T}{\partial t} + \vec{\nabla}.\left(-\lambda_m \vec{\nabla} T + \overrightarrow{\dot{m}_w} c_{p,w}(T - T_{ref}) + \overrightarrow{\dot{m}_v}\left[c_{p,v}(T - T_{ref}) + h_v\right]\right)}$$

$$\boldsymbol{= -\frac{\partial(\varepsilon_g \rho_v)}{\partial t} h_v} \quad \textbf{Eq. 6}$$

where ρ_m is the density of the material (kg.m^{-3}), $c_{p,m}$ is the thermal capacity of the material (J.kg^{-1}.K^{-1}), λ_m is the thermal conductivity of the material (W.m^{-1}.K^{-1}), $c_{p,w}$ is the thermal capacity of water (J.kg^{-1}.K^{-1}), T_{ref} is the reference temperature (273.15 K), $c_{p,v}$ is the thermal capacity of the vapour (J.kg^{-1}.K^{-1}), h_v is the vaporisation enthalpy (kJ.kg^{-1}) and ρ_v is the density of the vapour (kg.m^{-3})

2.3.2 General equations for bulk water, beaker and insulation

In the other parts of the system, the beaker, the bulk water and the outer insulation as well as the insulation between the water and the material, there is only heat transfer:

$$\rho_i c_i \frac{\partial T}{\partial t} + \vec{\nabla}.\left(-\lambda_i \vec{\nabla} T\right) = 0 \qquad \text{Eq. 7}$$

where ρ_i is the density (kg.m^{-3}), $c_{p.i}$ is the thermal capacity (J.kg^{-1}.K^{-1}) and λ_i is the thermal conductivity (W.m^{-1}.K^{-1}) of the component i (water, beaker or insulation).

2.3.3 Boundary conditions

At the surface boundary (Eq. 8), the heat exchange takes into account air convection, sunlight radiation and heat loss due to water evaporation. The latter involves the energy required for evaporation (enthalpy of vaporisation of water, h_v in J.kg^{-1}) multiplied by the evaporation rate $\dot{m}$ in kg.m^{-2}.h^{-1}.

$$-\vec{n}.\left(-\lambda_m \vec{\nabla} T\right) = h_c(T_a - T) + F_m[c_{p,v}(T - T_{ref}) + h_v] + P_s + E_m \sigma\left(T_a{}^4 - T^4\right) \qquad \text{Eq. 8}$$

with λ_m (W.m^{-1}.K^{-1}) the thermal conductivity of the material, h_c (W.m^{-2}.K^{-1}) the convection coefficient at the surface, T_a (K) the air temperature , E_m (dimensionless) the emissivity of the material and σ (5.67 ×10^{-8} W.m^{-2}.K^{-4}) the Stefan-Boltzmann constant. $-\vec{n}$ represents the unit vector normal to the boundary.

At the upper surface, water evaporation was described by the following equation:

$$-\vec{\mathbf{n}}.\left(\overrightarrow{\dot{\mathbf{m}}_{\mathbf{w}}}+\overrightarrow{\dot{\mathbf{m}}_{\mathbf{v}}}\right)=\mathbf{F_m} \quad \textbf{Eq. 9}$$

Finally, F_m was deduced from the difference between the water concentration at the material surface and the air and was calculated as follows [25]:

$$\mathbf{F_m}=-\mathbf{k_m}\frac{\mathbf{M}}{\mathbf{R}}\left(\frac{\mathbf{P_w^{v,sat}}}{\mathbf{T}}\mathbf{a_w}-\mathbf{H_R}\frac{\mathbf{P_a^{v,sat}}}{\mathbf{T_a}}\right) \quad \textbf{Eq. 10}$$

where M (18×10^{-3} kg.mol^{-1}) is the molar mass of water, R (8.314 J.mol^{-1}.K^{-1}) is the universal gas constant, $P_w^{v,sat}$ (Pa) and $P_a^{v,sat}$ (Pa) are the water vapour pressures at the local temperature, T (K), and at the air temperature, T_a (K), respectively, a_w (dimensionless) is the water activity, H_R (%) is the relative humidity and k_m (m.s^{-1}) is the convective mass exchange coefficient, calculated using the Colburn analogy [26]:

$$\mathbf{k_m}=\frac{\mathbf{h_c}}{\mathbf{1000}} \quad \textbf{Eq. 11}$$

Besides, $P_w^{v,sat}$ and $P_a^{v,sat}$ were calculated from the Clapeyron formula as follows:

$$\mathbf{P_x^{v,sat}}=\mathbf{P_0}\,\mathbf{exp}\left(\frac{\mathbf{h_v}}{\mathbf{R}}\mathbf{M}\left(\frac{\mathbf{1}}{\mathbf{T_0}}-\frac{\mathbf{1}}{\mathbf{T}}\right)\right) \quad \textbf{Eq. 12}$$

where P_0 is the reference pressure, 1 atm, and T_0 is the boiling point of water, 373.15 K.

The heat exchange between the air and the insulation takes place by convection and radiation:

$$-\vec{\mathbf{n}}.\left(-\boldsymbol{\lambda_i}\vec{\boldsymbol{\nabla}}\mathbf{T}\right)=\mathbf{h_{c,s}}(\mathbf{T_a}-\mathbf{T})+\mathbf{E_s}\boldsymbol{\sigma}\left(\mathbf{T_a}^{\mathbf{4}}-\mathbf{T}^{\mathbf{4}}\right) \quad \textbf{Eq. 13}$$

where λ_i is either λ_w, λ_b or λ_{im} depending on the location, $h_{c,s}$ (W.m^{-2}.K^{-1}) is the convection coefficient on the side and E_s (dimensionless) is the emissivity of the beaker side.

At the interface between the balance and the bottom of the insulation, only a convective heat flow was assumed:

$$-\vec{\mathbf{n}}.\left(-\boldsymbol{\lambda_b}\vec{\boldsymbol{\nabla}}\mathbf{T}\right)=\mathbf{h_{c,b}}(\mathbf{T_a}-\mathbf{T}) \quad \textbf{Eq. 14}$$

where $h_{c,b}$ (W.m^{-2}.K^{-1}) is the convection coefficient at the bottom of the beaker.

At the interface between the water and the material, as the material was considered saturated, the liquid fraction was set equal to the porosity, and thermal continuity was assumed.

$$\boldsymbol{\varepsilon_l = \varphi} \qquad \textbf{Eq. 15}$$

where φ is the porosity of the material.

The calculated variables, T and ε_l, were obtained by using the commercial software COMSOL Multiphysics 6.0. A mesh consisting of 1517 elements was used (**Figure 2b**) to model the entire system (beaker, insulation foams, water and evaporation material). The evaporating surface area was divided into smaller elements to have a better accuracy, and 59 elements were used for this purpose. The rest of the mesh was created automatically by the software, depending on the physics involved. An internal parametric study on the number of mesh elements was performed. The mesh presented here offers the most interesting compromise between simulation time and calculation accuracy. Using a desktop computer with two Xeon Silver 4214R CPUs (24 cores) combined with 256 GB of RAM, the model was computed in 48 seconds.

Table 1. Input parameters used in the simulation.

Symbols	Definitions	Units	Values
λ_w, λ_s, λ_a, λ_{im}, λ_b	Thermal conductivities of water, skeleton of the evaporation material, air, insulating material and beaker	W m^{-1} K^{-1}	0.6, 0.32, 0.0262, 0.043, 1.38
φ	Porosity of the evaporation material	-	0.955
$c_{p,w}$, $c_{p,v}$, $c_{p,s}$, $c_{p,im}$, $c_{p,b}$	Heat capacities of water, vapour, evaporation material, insulating material and beaker	J K^{-1} kg^{-1}	4180, 1890, 1800, 871, 703
D_w	Coefficient of diffusion of water inside the material	m^2 s^{-1}	10^{-8}
D_v	Coefficient of diffusion of vapour in the air	m^2 s^{-1}	2.82×10^{-5}
ρ_w, ρ_s, ρ_i	Density of water, skeleton density of the evaporation material and bulk density of the insulating material	kg m^{-3}	1000, 1550, 30
σ	Stefan-Boltzmann constant	W m^{-2} K^{-4}	5.67×10^{-8}

R	Universal gas constant	J mol^{-1} K^{-1}	8.314
M	Molar mass of water	kg mol^{-1}	0.01801
P_0	Standard pressure	Pa	101325
T_0	Boiling point of water	K	373.15
T_a	Air temperature	K	293.15
T_{ref}	Reference temperature	K	273.15
$h_c, h_{c,b}$	Heat transfer coefficients at the surface and the bottom	W m^{-2} K^{-1}	10, 1
E_m	Emissivity of the material	-	1
H_r	Relative humidity	-	0.5
τ_o	Tortuosity	-	1.3

3 RESULTS AND DISCUSSION

3.1 MODEL VALIDATION

In order to validate the model, experiments were conducted and the ambient conditions of these experiments (T_a and H_r) were set as parameters in the simulation. **Figure 3** shows the simulated and experimental results of the temperature, measured at the evaporation surface, as well as the simulated and experimental evolution of the water mass of over time.

During the first phase of illumination, the evaporation rate is 1.17 $kg.m^{-2}.h^{-1}$ and the average surface temperature reaches 35°C after the three-hour period. During the second period, when the sunlight is switched off, the evaporation rate is 0.34 $kg.m^{-2}.h^{-1}$ and the average surface temperature after three hours is about 18°C. Overall, the cycles are well visible and the simulation fits for the evolution of the water mass well. The calculated surface temperature shows a slight difference, which is due to temperature variations. We can therefore validate the model and conclude that it can be used to simulate the behaviour of the evaporation system over time.

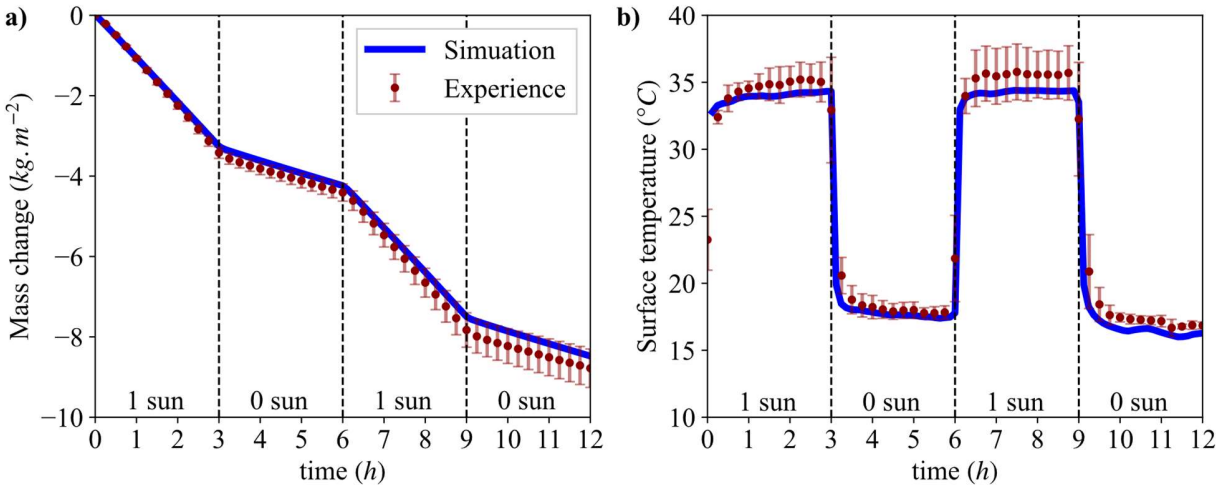

Figure 3. (a) Experimental (red dots) and simulated (blue line) mass changes, and (b) experimental (red dots) and simulated (blue lines) surface temperature for a 12h experiment with alternating periods of sunlight and darkness of 3 hours each.

3.2 PARAMETRIC STUDY

3.2.1 Solar flux absorption coefficient

One parameter that can vary depending on the type of material is the absorption of sunlight by its surface. Typically, materials achieve absorption values above 95% for maximum solar energy utilisation [2,27,28]. A parametric study was conducted to investigate the impact of this parameter on performance.

Figure 4a shows the evaporation rate and efficiency as a function of surface absorption of sunlight. A gain of 0.1 in sunlight absorption results directly in a gain of 0.1 $kg.m^{-2}.h^{-1}$ in evaporation rate and 5% in efficiency. This represents a loss of evaporation performance of 11%, which means that the improvement in surface absorption makes sense.

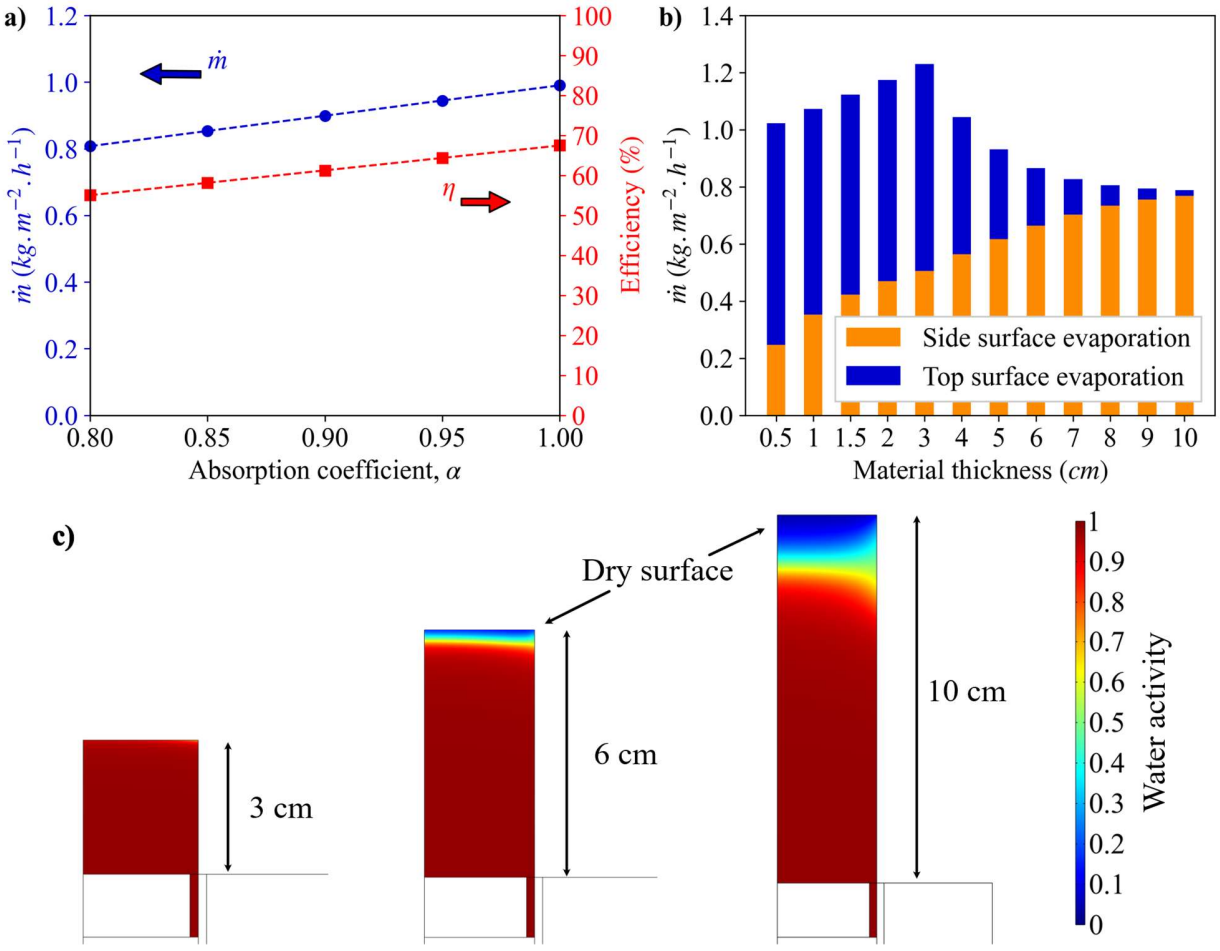

Figure 4. (a) Simulated evaporation rate and efficiency for different solar flux absorption coefficients; and (b) simulated top and lateral evaporation rates for different values of porous structure thickness. (c) Simulated maps of water activity in the foam for three different heights (3 cm, 6 cm and 10 cm).

3.2.2 Thickness of the porous structure

Some types of materials allow for different thicknesses to be chosen during manufacture. Wood, for instance, can be set to a certain thickness [29], while a lotus leaf has a fixed thickness [11,30]. For a material with a controlled thickness (wood, foam etc.), there is an optimal value for its use as an evaporation material. **Figure 4b** shows the simulated evaporation rate and efficiency as a

function of thickness, from half a centimetre to several centimetres. Overall, the evaporation rate increases with the material thickness, but a local maximum can be seen at 3 cm. This is due to the fact that, with increasing material height, water transport starts to be a limiting factor. In addition, the thicker the foam, the higher the evaporation area. Thus, until water transport becomes a limiting factor, the evaporation rate increases. For thicknesses greater than 3 cm, water transport is limited, so that only lateral evaporation increases until a maximum is reached and water can no longer progress through the foam. However, this does not increase the overall evaporation rate since the evaporation rate at the surface decreases with thickness This is clearly visible in **Figure 4c** for the 6 cm and 10 cm cases. The water activity at the surface is low, meaning that the surface is dry. For 3 cm, the water activity is still close to 1, so evaporation is still possible. The increase in evaporation with thickness up to a certain point correlates with recent studies that have been conducted to harness the maximum transportability of water [16].

3.2.3 Diffusion coefficient of liquid water

Diffusion within the evaporative material is essential, because even if energy management at the surface is effective, insufficient water will prevent evaporation from occurring, as it has been shown in 3.2.2. To simulate the unavailability of water at the surface, a parametric study of the water diffusion coefficient within the porous structure was conducted.

Figure 5a shows the results of the evaporation rate and efficiency as a function of the diffusion coefficient. Little change is visible when water transport is sufficient (above 10^{-9} $m.s^{-1}$). However, below this value of diffusion coefficient, the evaporation rate is strongly impacted by the limited water transport, decreasing from 1.0 $kg.m^{-2}.h^{-1}$ to 0.6 $kg.m^{-2}.h^{-1}$ for a diffusion coefficient of 10^{-9} $m.s^{-1}$ and 10^{-10} $m.s^{-1}$, respectively. This phenomenon can be explained by the fact that, with a low diffusion coefficient, the water does not reach the surface (**Figure 5d)**, resulting in a decrease in

evaporated flux (**Figure 5b)** and an increase in surface temperature (**Figure 5c)**. After 2 hours, the surface of the foam is completely dry for a diffusion coefficient of less than 10^{-9} m.s^{-1}, while the water uptake stabilises at 86%, which still allows water to reach the surface, for a coefficient of 10^{-9} m.s^{-1}.

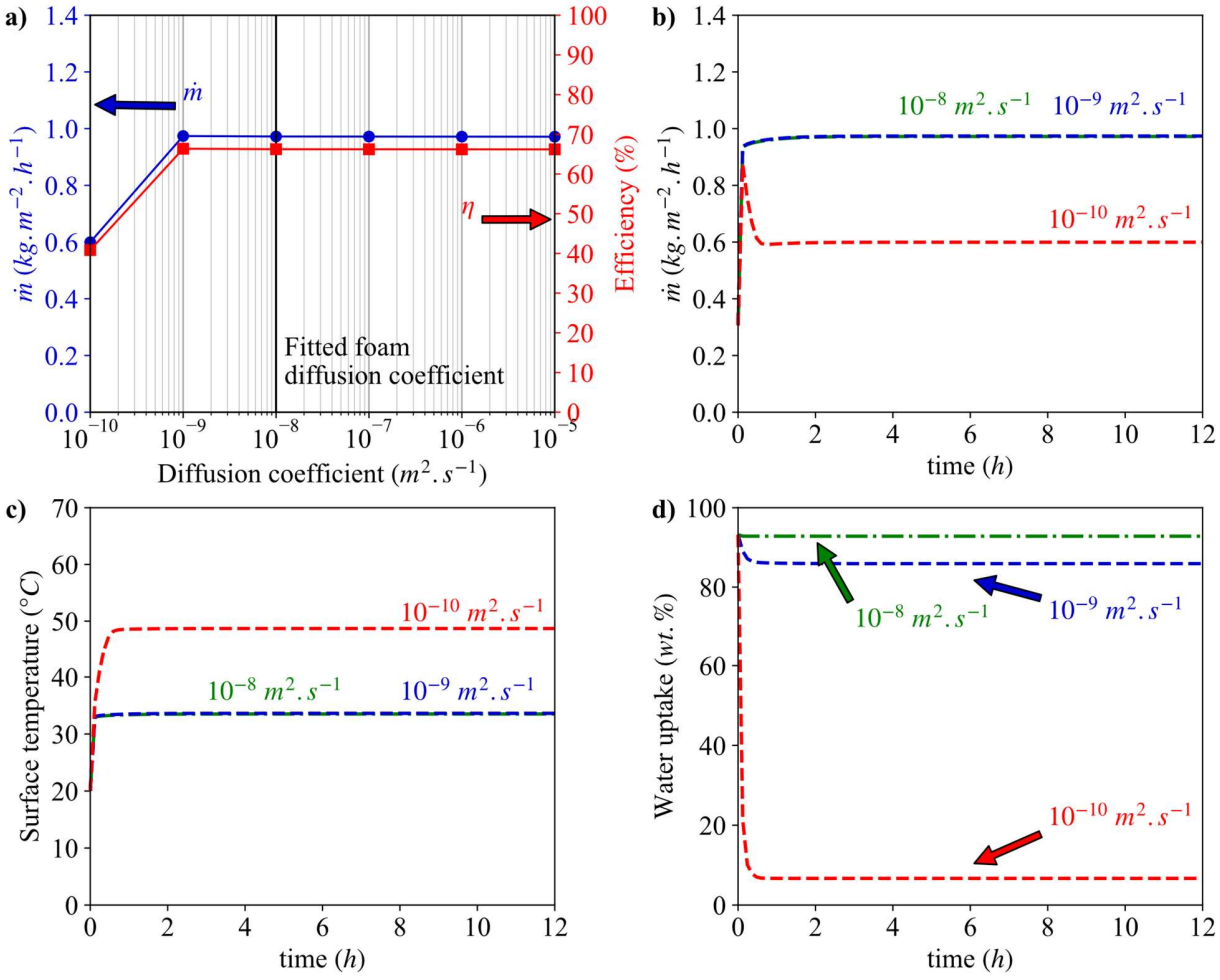

Figure 5. (a) Simulated evaporation rate and efficiency for different values of water diffusion coefficient; and (b) transient evolution of evaporation rate; (c), surface temperature; and (d) water uptake for different values of the water diffusion coefficient.

3.2.4 Thickness of the insulating wall

Since external conditions affect evaporation performance [21], it may be worthwhile to add a layer of insulating foam to focus on studying the performance of the material at the surface where evaporation occurs. **Figure 6a** shows the performance of the system as a function of the thickness of the insulating foam, with a thermal conductivity of 0.043 $W.m^{-1}.K^{-1}$, around the beaker. The evaporation rate increases until it stabilises at about 1.04 $kg.m^{-2}.h^{-1}$, which represents a 4% increase compared to the system without thermal insulation. This is due to the fact that energy is no longer lost through the sides of the material, which increases the surface temperature and thus the evaporation rate (**Figure 6b**). However the increase is minimal compared to a previous study [21], because an additional insulating layer is used between the water and the evaporating material. Exchanges through the side of the beaker are carried out with already insulated bulk water.

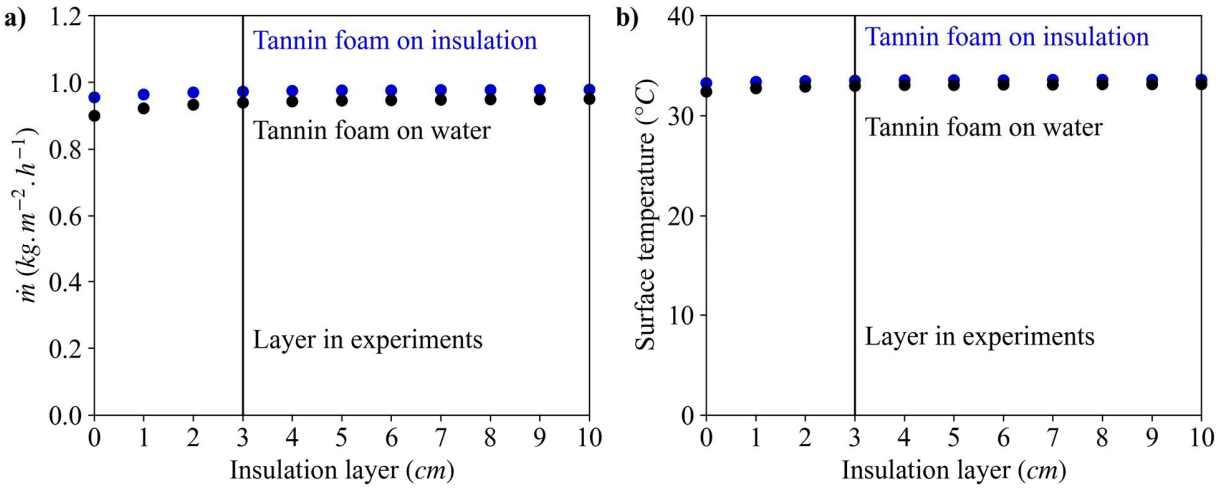

Figure 6. (a) Evaporation rate and efficiency; and (b) surface temperature as a function of the thickness of the insulation around the beaker (0 cm is the case without insulation, and the vertical line represents the case for a 3 cm insulating layer, used in the experiment).

3.3 Water evaporation potential

In the literature, experimental measurements are performed in a controlled environment with constant simulated solar radiation, or outdoors in a chamber (or under a bell jar or in a solar still) subjected to solar radiation that varies throughout the day. This section proposes to simulate the behaviour of the evaporator illuminated by real solar radiation and to estimate the potential water evaporation of this system if it were located in large cities in the northern hemisphere.

3.3.1 Temporal evolution in Paris

Figure 7 shows the evolution of solar radiation, efficiency, surface temperature and evaporation rate for four 21st of the month, from winter to summer solstice. Sunshine data from Paris (France – Latitude 48°51′12″) were used [31] as well as air temperature and humidity data throughout 2021 [32]. As expected, the evaporation rate increases with solar radiation. It should be noted that a phase shift is observed between the solar radiation and the evaporated flux. Indeed, the maximum evaporation does not occur at the time when the solar flux is the most important, the maximum is at 13h for evaporation while the solar flux is maximum at 12h. It should be noted that solar time is considered here, i.e., for which the sun is at its zenith at noon. Considering the calculation of the efficiency (Eq. 1), the value calculated at the beginning and end of the day is inconsistent because it implies a sunshine close to 0. Nevertheless, an overall increase in efficiency is observable during the day and is maximal in the afternoon (**Figure 7b**). The increase in efficiency at the beginning and end of the day can be explained by Eq. 1, which shows a decreasing illumination until it reaches zero, thus mathematically increasing the efficiency value. This phenomenon and the observed phase shift are due to the temperature at the evaporation surface increasing with the concentration of solar radiation (**Figure 7a**) and the thermal energy stored in the material (**Figure 7c**), which

enhances evaporation (Eq. 10 and Eq. 12). The total potential evaporation on a summer day (21st June) is 12 L per m^2 of the present tannin foam.

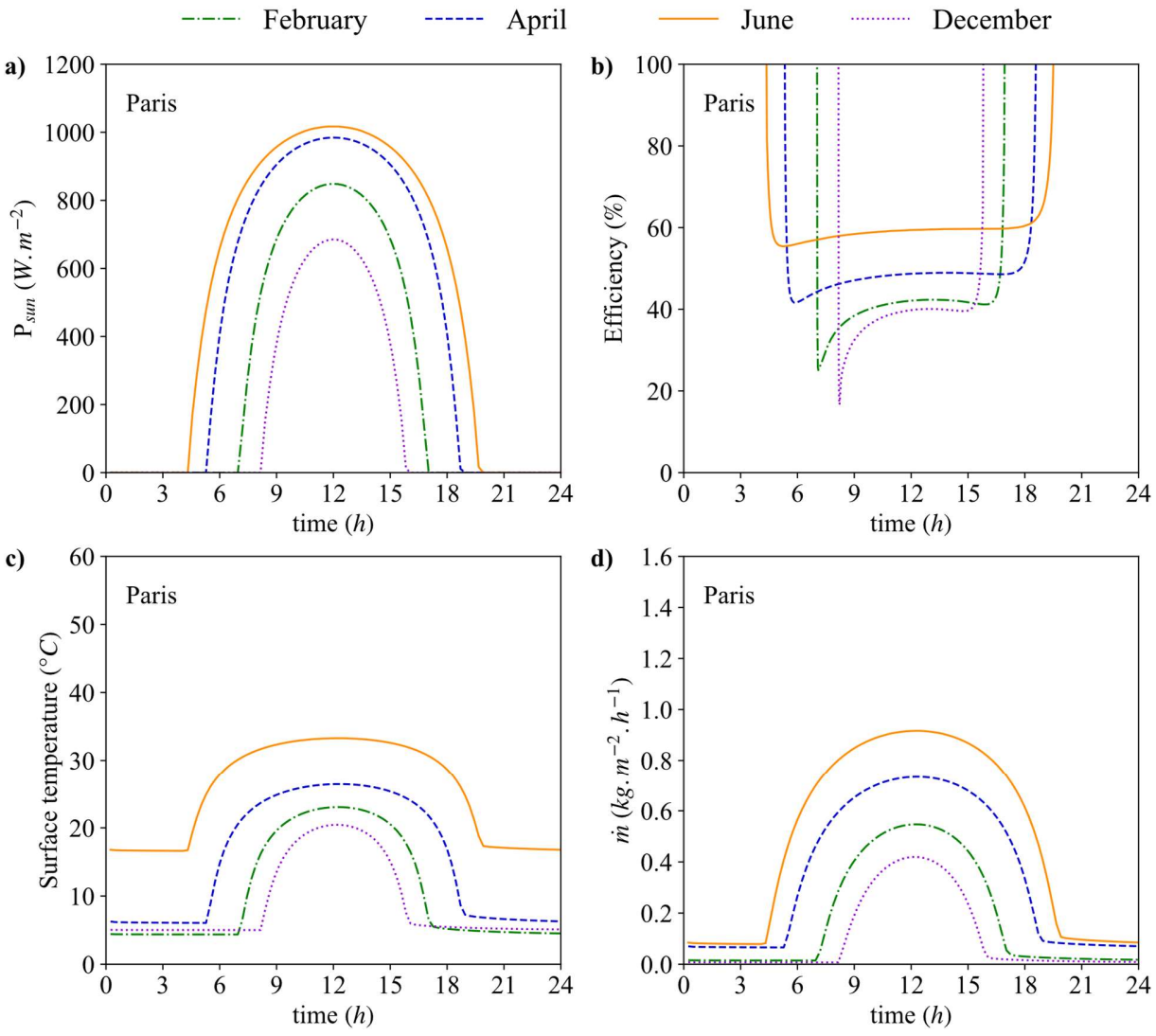

Figure 7. (a) Simulated hourly evolution of solar radiation; (b) efficiency; (c) surface temperature and (d) evaporation rate in Paris (France – Latitude 48°51′12″). Four 21st of the month were selected over the year: December, February, April, June.

3.3.2 Annual potential water evaporation for different locations on earth

Figure 8 shows the annual and monthly evaporation per unit area simulated for different locations on the planet. In these calculations, direct radiation is changed as well as local air temperature and humidity, taken throughout the year [32]. The monthly calculation was made for a typical day corresponding to the 21st of the month in order to take into account the summer and winter solstices. The annual calculation was performed by summing the evaporated quantities of all months of the year, the monthly value being considered constant. The monthly results show significant variations with the latitude of the city studied. Indeed, cities located near the poles show almost no evaporation during winter and evaporation close to other latitudes during the summer, since the sun shines almost all day in Reykjavik in summer time, for example (**Figure 9a**). On the contrary, cities located near the equator offer similar evaporation performance all year round, about 8.5 kg.m^{-2} for Quito from December to June, which is due to the constant illumination throughout the year (**Figure 9g**). Indeed, between the northernmost capital city, Reykjavík, and a city located on the equator, Quito, there is a 76% increase in annual evaporation. However, evaporation is not only related to latitude, as local ambient conditions, relative humidity and temperature also have a significant impact on evaporation, as has been shown previously [21]. Dubai, for instance, is located 25° north of Quito and has a 72% higher annual evaporation, which is due to the fact that the local air is much drier and the average temperature is higher throughout the year, as shown in **Figure 9e** and **Figure 9h**.

In **Figure 8b**, we can observe that the simulated annual freshwater production increases at low latitudes with an arid climate, with the highest theoretical evaporation located in Dubai with 5342 kg.m^{-2}, followed by Cairo with 4723 kg.m^{-2}. For the other cities selected, Beijing, Paris or Moscow, evaporation decreases with latitude. **Figure 8d** shows that the annual amount of water produced is

not directly linear with latitude, as warmer climates have higher evaporation values compared to the trend observed for other cities as a function of latitude. This Figure shows that there can be a dispersion in the amount of water recovered for the same latitude. **Figure 8e** shows that the main factor impacting on the amount of water produced is temperature with a linear trend with the annual average temperature and therefore with the climate.

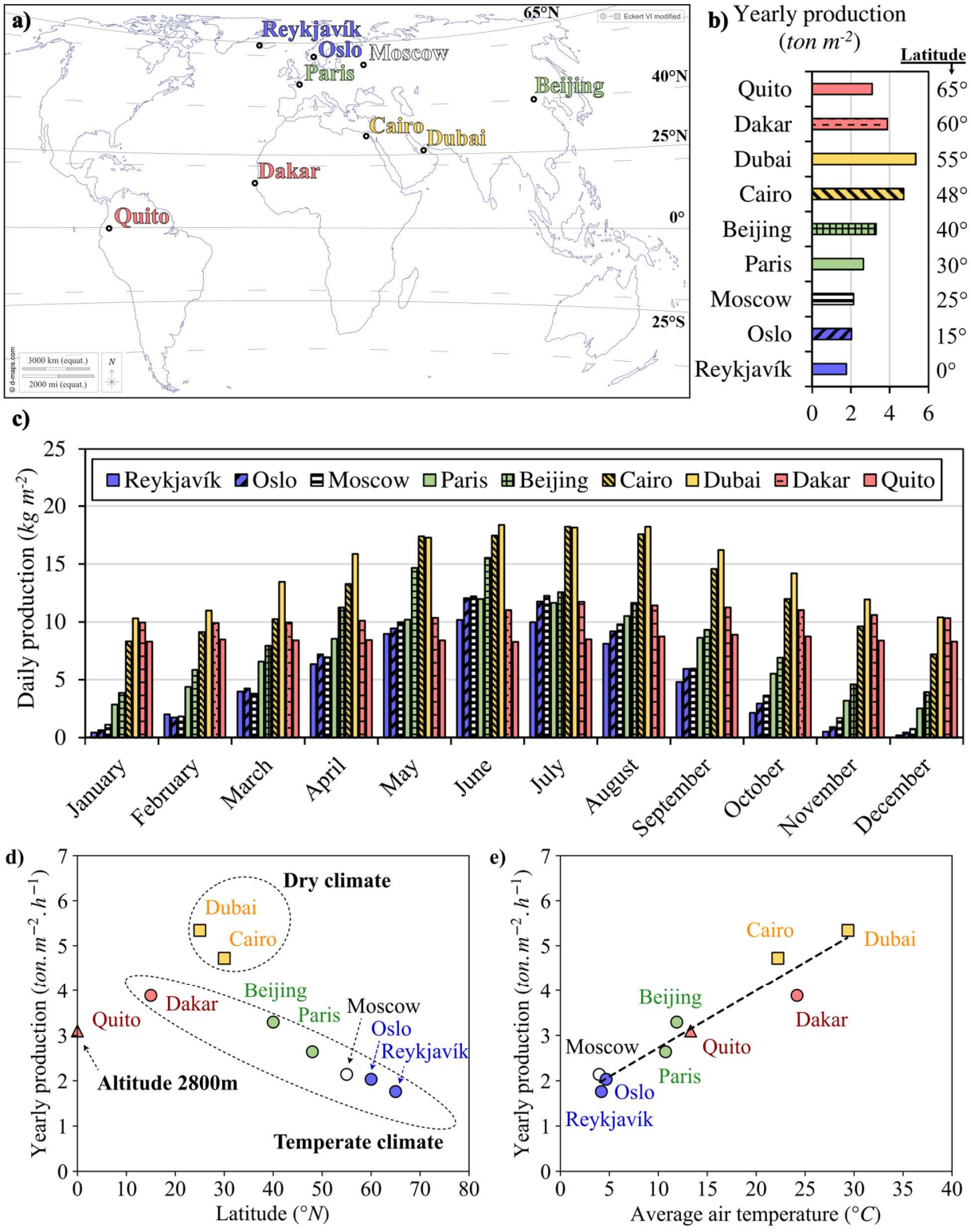

Figure 8. (a) Map [33] of locations used to estimate simulated (b) yearly and (c) monthly evaporation per unit area over the planet (air temperature and relative humidity are set to local

values throughout the year [32]); simulated annual water production as a function of (d) latitude and climate: Dry climate, Dubai and Cairo, ◻; High altitude climate, Quito, △, and Temperate Climate, all others ○ (colours as in a); and of (e) the average air temperature the for the cities studied.

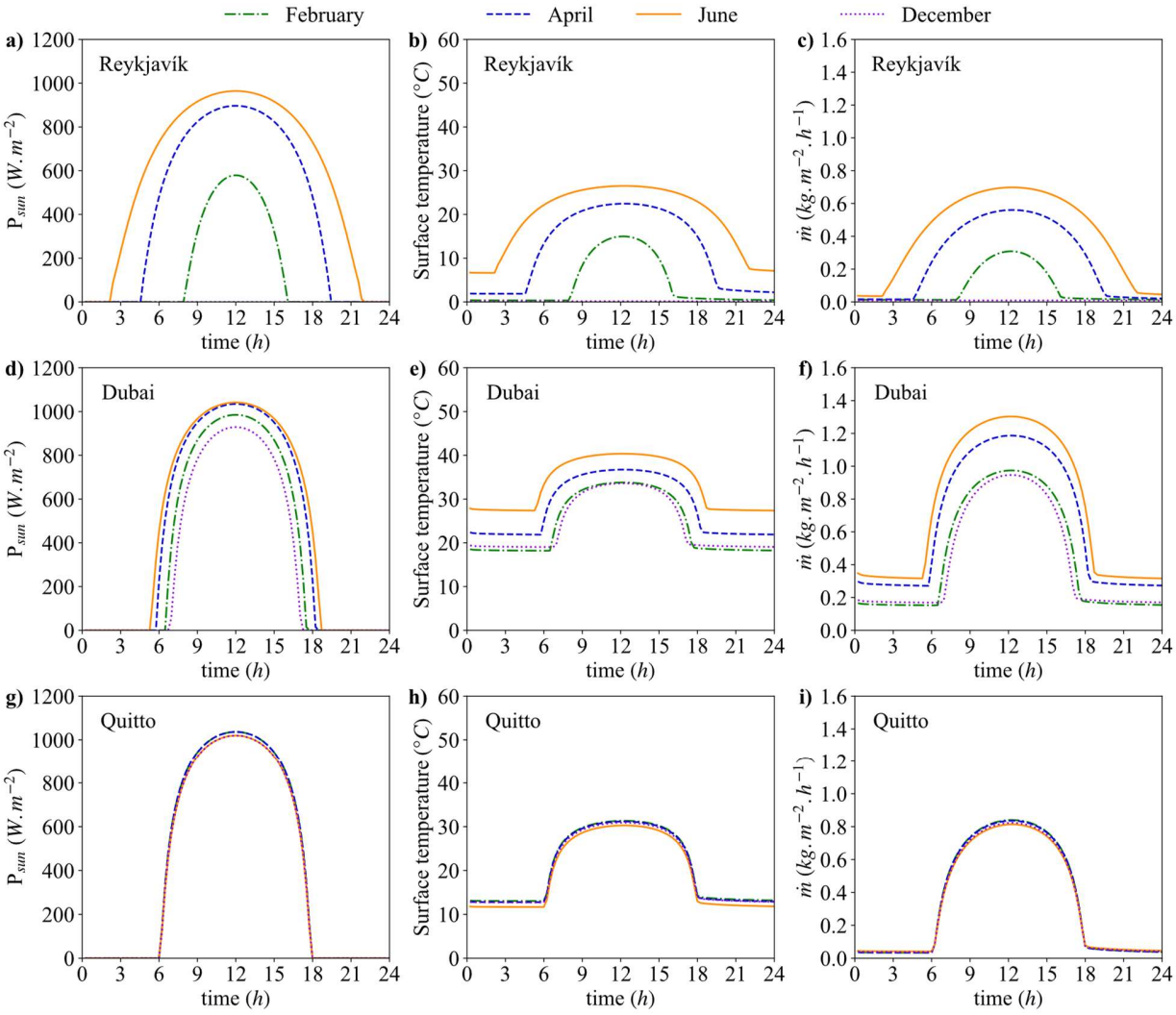

Figure 9. Simulated evolution of: (a), (d) and (g) solar radiation; (b), (e) and (h) surface temperature; and (c), (f) and (i) evaporation rate in Reykjavik (top), Dubai (middle) and Quito (bottom).

4 Conclusions

Using a two-dimensional axisymmetric model that was validated for temperature and water mass changes as a function of time, several phenomena were explored. These included the effect of three material properties: water diffusion coefficient, material thickness and surface light absorption coefficient. Foam thickness, diffusion coefficient and light absorption have been shown to be key factors. By increasing the area available for evaporation, thickness directly increases the performance until the material can no longer diffuse water. The diffusion coefficient allows for the presence of liquid water, because if it is too low, not enough water can be transported to the surface, and light absorption improves energy consumption and therefore performance. The study of the thickness of insulation around the measuring system shows that evaporation is no longer improved above a certain thickness and that the presence of insulation between the bulk water and the evaporation surface decreases the usefulness of the added insulating layer around the beaker.

A typical summer day in Paris was also evaluated, and we show that the theoretical potential amount of water evaporated would be 12 L per m^2 of foam area, using the (non-optimised) rigid foam used here to validate the model. The simulated evolution of the evaporation rate at different locations of the planet shows that latitude has a significant impact on the performance in winter. Ambient temperature and humidity conditions also play a major role in evaporation performance. Dubai, for instance, is located 25° north of Quito and has 72% higher annual evaporation, which is due to the fact that the local air is much drier and the average temperature is higher throughout the year.

5 ACKNOWLEDGEMENT

This work was partially supported by the French Ministry of the Armed Forces - Defence Innovation Agency and the TALiSMAN2 project (ERDF-LO0022687). This study was presented

and published in the proceedings of the 15th International Conference on Heat Transfer, Fluid Mechanics and Thermodynamics (HEFAT2021), online, 26 – 28 July 2021.

REFERENCES

[1] C. Chen, Y. Kuang, L. Hu, Challenges and Opportunities for Solar Evaporation, Joule. 3 (2019) 683–718. https://doi.org/10.1016/j.joule.2018.12.023.

[2] P. Zhang, Q. Liao, H. Yao, Y. Huang, H. Cheng, L. Qu, Direct solar steam generation system for clean water production, Energy Storage Materials. 18 (2019) 429–446. https://doi.org/10.1016/j.ensm.2018.10.006.

[3] F. Zhao, Y. Guo, X. Zhou, W. Shi, G. Yu, Materials for solar-powered water evaporation, Nat Rev Mater. (2020) 1–14. https://doi.org/10.1038/s41578-020-0182-4.

[4] S. Meng, X.-J. Zha, C. Wu, X. Zhao, M.-B. Yang, W. Yang, Interfacial Radiation-Absorbing Hydrogel Film for Efficient Thermal Utilization on Solar Evaporator Surfaces, Nano Lett. 21 (2021) 10516–10524. https://doi.org/10.1021/acs.nanolett.1c04066.

[5] Hierarchically structured evaporator with integrated water supply and evaporation layers to retard salt accumulation - ScienceDirect, (n.d.). https://www-sciencedirect-com.bases-doc.univ-lorraine.fr/science/article/pii/S0017931021015453?dgcid=rss_sd_all (accessed March 28, 2022).

[6] Md.N.A.S. Ivan, A.M. Saleque, S. Ahmed, P.K. Cheng, J. Qiao, T.I. Alam, Y.H. Tsang, Waste Egg Tray and Toner-Derived Highly Efficient 3D Solar Evaporator for Freshwater Generation, ACS Appl. Mater. Interfaces. 14 (2022) 7936–7948. https://doi.org/10.1021/acsami.1c22215.

[7] V.K. Dwivedi, G.N. Tiwari, Experimental validation of thermal model of a double slope active solar still under natural circulation mode, Desalination. 250 (2010) 49–55. https://doi.org/10.1016/j.desal.2009.06.060.

[8] J.T. Mahdi, B.E. Smith, A.O. Sharif, An experimental wick-type solar still system: Design and construction, Desalination. 267 (2011) 233–238. https://doi.org/10.1016/j.desal.2010.09.032.

[9] S.K. Hota, G. Diaz, Activated carbon dispersion as absorber for solar water evaporation: A parametric analysis, Solar Energy. 184 (2019) 40–51. https://doi.org/10.1016/j.solener.2019.03.080.

[10] H. Li, S. Wang, Z. Yan, X. Niu, X. Sun, W. Hong, Harvesting conductive heat loss of interfacial solar evaporator for thermoelectric power generation, Applied Thermal Engineering. 208 (2022) 118279. https://doi.org/10.1016/j.applthermaleng.2022.118279.

[11] Y. Liao, J. Chen, D. Zhang, X. Wang, B. Yuan, P. Deng, F. Li, H. Zhang, Lotus leaf as solar water evaporation devices, Materials Letters. 240 (2019) 92–95. https://doi.org/10.1016/j.matlet.2018.12.133.

[12] N. Xu, X. Hu, W. Xu, X. Li, L. Zhou, S. Zhu, J. Zhu, Mushrooms as Efficient Solar Steam-Generation Devices, Advanced Materials. 29 (2017) 1606762. https://doi.org/10.1002/adma.201606762.

[13] X. Li, W. Xu, M. Tang, L. Zhou, B. Zhu, S. Zhu, J. Zhu, Graphene oxide-based efficient and scalable solar desalination under one sun with a confined 2D water path, PNAS. 113 (2016) 13953–13958. https://doi.org/10.1073/pnas.1613031113.

[14] X.-F. Zhang, Z. Wang, L. Song, Y. Feng, J. Yao, Chinese ink enabled wood evaporator for continuous water desalination, Desalination. 496 (2020) 114727. https://doi.org/10.1016/j.desal.2020.114727.
[15] J. Li, X. Zhou, G. Chen, F. Wang, J. Mao, Y. Long, H. Sun, Z. Zhu, W. Liang, A. Li, Evaporation efficiency monitoring device based on biomass photothermal material for salt-resistant solar-driven interfacial evaporation, Solar Energy Materials and Solar Cells. 222 (2021) 110941. https://doi.org/10.1016/j.solmat.2020.110941.
[16] C.T.K. Finnerty, A.K. Menon, K.M. Conway, D. Lee, M. Nelson, J.J. Urban, D. Sedlak, B. Mi, Interfacial Solar Evaporation by a 3D Graphene Oxide Stalk for Highly Concentrated Brine Treatment, Environ. Sci. Technol. 55 (2021) 15435–15445. https://doi.org/10.1021/acs.est.1c04010.
[17] Y. Xu, J. Xu, J. Zhang, X. Li, B. Fu, C. Song, W. Shang, P. Tao, T. Deng, All-in-one polymer sponge composite 3D evaporators for simultaneous high-flux solar-thermal desalination and electricity generation, Nano Energy. 93 (2022) 106882. https://doi.org/10.1016/j.nanoen.2021.106882.
[18] Y. Wang, X. Wu, P. Wu, J. Zhao, X. Yang, G. Owens, H. Xu, Enhancing solar steam generation using a highly thermally conductive evaporator support, Science Bulletin. 66 (2021) 2479–2488. https://doi.org/10.1016/j.scib.2021.09.018.
[19] F. Zhao, X. Zhou, Y. Shi, X. Qian, M. Alexander, X. Zhao, S. Mendez, R. Yang, L. Qu, G. Yu, Highly efficient solar vapour generation via hierarchically nanostructured gels, Nature Nanotech. 13 (2018) 489–495. https://doi.org/10.1038/s41565-018-0097-z.
[20] A.K. Menon, I. Haechler, S. Kaur, S. Lubner, R.S. Prasher, Enhanced solar evaporation using a photo-thermal umbrella for wastewater management, Nat Sustain. 3 (2020) 144–151. https://doi.org/10.1038/s41893-019-0445-5.
[21] R. Fillet, V. Nicolas, V. Fierro, A. Celzard, Modelling heat and mass transfer in solar evaporation systems, International Journal of Heat and Mass Transfer. 181 (2021) 121852. https://doi.org/10.1016/j.ijheatmasstransfer.2021.121852.
[22] X. Li, G. Ni, T. Cooper, N. Xu, J. Li, L. Zhou, X. Hu, B. Zhu, P. Yao, J. Zhu, Measuring Conversion Efficiency of Solar Vapor Generation, Joule. 3 (2019) 1798–1803. https://doi.org/10.1016/j.joule.2019.06.009.
[23] G. Tondi, V. Fierro, A. Pizzi, A. Celzard, Tannin-based carbon foams, Carbon. 47 (2009) 1480–1492. https://doi.org/10.1016/j.carbon.2009.01.041.
[24] Z. Marie, V. Nicolas, A. Celzard, V. Fierro, First approach for modelling the physical foaming of tannin-based thermoset foams, International Journal of Thermal Sciences. 149 (2020) 106212. https://doi.org/10.1016/j.ijthermalsci.2019.106212.
[25] V. Nicolas, F. Vanin, D. Grenier, T. Lucas, C. Doursat, D. Flick, Modeling bread baking with focus on overall deformation and local porosity evolution, AIChE Journal. 62 (2016) 3847–3863. https://doi.org/10.1002/aic.15301.
[26] Y. CENGEL, Heat Transfer a practical approach, Second Edition, 2002.
[27] C. Du, C. Huang, A floating vapor condensation structure in a heat-localized solar evaporation system for facile solar desalination, Applied Thermal Engineering. 201 (2022) 117834. https://doi.org/10.1016/j.applthermaleng.2021.117834.
[28] Biomimetic Hybridization of Janus-like Graphene Oxide into Hierarchical Porous Hydrogels for Improved Mechanical Properties and Efficient Solar Desalination Devices | ACS Nano, (n.d.). https://pubs-acs-org.bases-doc.univ-lorraine.fr/doi/10.1021/acsnano.1c07391 (accessed January 18, 2022).

[29] Z. Yu, S. Cheng, C. Li, Y. Sun, B. Li, Enhancing efficiency of carbonized wood based solar steam generator for wastewater treatment by optimizing the thickness, Solar Energy. 193 (2019) 434–441. https://doi.org/10.1016/j.solener.2019.09.080.
[30] J. Fang, J. Liu, J. Gu, Q. Liu, W. Zhang, H. Su, D. Zhang, Hierarchical Porous Carbonized Lotus Seedpods for Highly Efficient Solar Steam Generation, Chem. Mater. 30 (2018) 6217–6221. https://doi.org/10.1021/acs.chemmater.8b01702.
[31] C.B.Honsberg, S.G.Bowden, Photovoltaics Education Website, (2019). https://www.pveducation.org/.
[32] Global Modeling and Assimilation Office (GMAO), MERRA-2 tavg1_2d_slv_Nx: 2d,1-Hourly,Time-Averaged,Single-Level,Assimilation,Single-Level Diagnostics V5.12.4, Greenbelt, MD, USA, Goddard Earth Sciences Data and Information Services Center (GES DISC), Accessed 06/12/2021 DOI:10.5067/VJAFPLI1CSIV, (2015).
[33] d-maps, Planisphere World (Europe Africa), (2022). https://d-maps.com/index.php?lang=en.